

Shape Programmable and Multifunctional Soft Textile Muscles for Wearable and Soft Robotics

Trung Thien Hoang,* Chi Cong Nguyen, Phuoc Thien Phan, James Davies, Hien Anh Tran, Mai Thanh Thai, Vi Khanh Truong, Tuan-Khoa Nguyen, Tat Thang Vo-Doan, Hoang-Phuong Phan, Nigel Hamilton Lovell, and Thanh Nho Do*

Textiles are promising candidates for use in soft robots and wearable devices due to their inherent compliance, high versatility, and skin comfort. Planar fluidic textile-based actuators exhibit low profile and high conformability, and can seamlessly integrate additional components (e.g., soft sensors or variable stiffness structures [VSSs]) to create advanced, multifunctional smart textile actuators. In this article, a new class of programmable, fluidic soft textile muscles (STMs) that incorporate multilayered silicone sheets with embedded fluidic channels is introduced. The STMs are scalable and fabricated by apparel engineering techniques, offering a fabrication approach able to create large-scaled multilayered structures that can be challenging for current microfluidic bonding methods. They are also highly automation compatible due to no manual insertion of elastic tubes/bladders into textile structures. Liquid metal is employed for creating fluidic channels. It is not only used for actuation but also used as channels for additional features such as soft piezoresistive sensors with enhanced sensitivity to STMs' pressure-induced elongation, or VSSs of either low-melting-point alloys or a new thermo-responsive epoxy with low viscosity and transition temperature. The STMs hold promising prospects for soft robotic and wearable applications, which is demonstrated by an example of a textile-based wearable 3D skin-stretch haptic interface.

1. Introduction

Soft robotics is an emerging field that has enabled a number of novel applications in robotics (e.g., grasping,^[1] locomotion,^[2] or foldable robots^[3]), healthcare,^[4] search and rescues,^[5] and wearable devices (e.g., haptics,^[6] rehabilitation,^[7] or assistance^[8]). Textiles have long been a familiar material with which we spend most of our lives in close proximity. They can be present in our daily lives in various forms, ranging from our clothing and garments to our bags, bedsheets, or bandages. However, for a long time, textiles have only been used as a passive constituent component in these items. Recently, textiles have been adopted for a new role as the material of choice for soft robots and medical devices thanks to their advantages of being lightweight, inherently flexible, and resilient against abrasion, crushing, and tearing. In addition, textiles' gentle touch on human skin can promote garment comfort and is ideal for developing wearable robots,

T. T. Hoang, C. C. Nguyen, P. T. Phan, J. Davies, H. A. Tran, N. H. Lovell, T. N. Do
Graduate School of Biomedical Engineering
Faculty of Engineering
Tyree Institute of Health Engineering (IHealthE)
UNSW
Sydney, New South Wales 2052, Australia
E-mail: z5275787@zmail.unsw.edu.au; tn.do@unsw.edu.au

M. T. Thai
College of Engineering and Computer Science
VinUniversity
Hanoi 100000, Vietnam

 The ORCID identification number(s) for the author(s) of this article can be found under <https://doi.org/10.1002/aisy.202300875>.

© 2024 The Authors. Advanced Intelligent Systems published by Wiley-VCH GmbH. This is an open access article under the terms of the Creative Commons Attribution License, which permits use, distribution and reproduction in any medium, provided the original work is properly cited.

DOI: 10.1002/aisy.202300875

V. K. Truong
Biomedical Nanoengineering Laboratory
College of Medicine and Public Health
Flinders University
Adelaide, South Australia 5042, Australia

T.-K. Nguyen
Queensland Micro and Nanotechnology Centre
Griffith University
Brisbane, Queensland 4111, Australia

T. T. Vo-Doan
School of Mechanical & Mining Engineering
The University of Queensland
St Lucia, Queensland 4072, Australia

H.-P. Phan
School of Mechanical and Manufacturing Engineering
Faculty of Engineering
UNSW
Sydney, New South Wales 2052, Australia

medical devices, and flexible sensing platforms.^[9] Textiles are also commercially available with a wide selection of material properties, which supports rapid prototyping processes and the transition of devices from the research environment to end products. Given these versatile characteristics and the unique design space, incorporating textiles into robots to form soft textile robotic systems can lead to a wide range of novel applications in smart adaptive clothing, protective garments, haptic and assistance devices, deployable shelters, or shape-changing structures.^[10]

Many actuation methods have been introduced to turn textiles into soft robots. For example, cables driven by electric motors have been used with textiles to create soft textile wearable devices and robots, such as soft exoskeletons for limb assistance,^[11] soft wearable gloves for finger manipulation,^[12] or haptics interfaces.^[13] In these cable-driven robotic systems, textiles are normally used as passive substrates to provide a comfortable and conformal fit to the users, anchor other components (e.g., motors, sensors, and power supplies), route cables, and direct forces. Despite high force and speed, which can be suitable for high-speed applications,^[10b,14] the cable-driven mechanism still has challenges, being heavy and bulky (from DC motors and power supplies) and needing sophisticated control for frictional loss compensation. Another popular mechanism to robotize textiles is based on thermo-responsive yarns, such as shape memory alloys or thermoplastic fibers and coils that contract under high temperatures and recover when cooling down. These thermo-responsive yarns can be incorporated directly with textile structures via traditional apparel techniques such as sewing, knitting, or weaving, resulting in a variety of textile robotic systems such as self-fitting wearables,^[15] haptic interfaces,^[16] or shape-changing robots.^[10a] Despite having relatively high strain and force generation, and suitable dimensions for incorporation with textile structures, the use of thermal excitation generally causes these yarns to have low efficiency and slow actuation speeds (mainly due to the cooling process). The requirement for relatively high actuation temperatures of a few fibers and coils^[10b,17] is also a concern for skin-contact devices based on this mechanism.

Fluidic actuation is one of the most investigated methods to create soft textile robotic systems where actuation relies on fluidic textile actuators or muscles. Fluidic textile actuators generally consist of inflatable chambers (i.e., bladders, tubes) inserted inside textile-based constraining structures where mechanical properties of textiles (e.g., stretchability^[18]) or textile structural designs (e.g., pleating or gathering^[19]) are employed to program the motions of the actuators. Upon pressurization from a fluid source (i.e., pneumatic or hydraulic), fluidic textile actuators can generate force and undergo shape changes (e.g., elongation, bending, or twisting) according to their compositions and configurations. Compared with other actuation mechanisms for textile-based soft robots, fluidic actuation can generate large forces and strains, has inherent compliance and diverse motions, and is simple to fabricate and control.^[10b,20] Braided pneumatic artificial muscles (PAMs or McKibben muscles) are one typical example of this type of actuator, where a braided mesh shell is used to constrain and convert the inflation of a stretchable bladder into radial expansion and axial contraction,^[21] which have been exploited in a number of soft textile robotic systems.^[22]

In addition to braided mesh shells, other variations of PAMs have also been developed based on knitted textile sleeves,^[23] bladder-free heat-sealed pouches,^[24] or constraining fibers that result in pressure-induced axial extension (as opposed to contraction) in inverse PAMs (or IPAMs).^[8,25]

In contrast to typically uniaxial and tubular forms of prior actuators, planar variants of fluidic textile actuators, inspired by natural instances where actuation can be achieved by sheetlike structures (e.g., human trapezius muscle or a curling dry maple leaf), have also been developed for low profile and flexibility goals. The multi-pouch PAMs (i.e., inflatable servo) rely on an array of linearly connected inflatable pouches that can transform from flat to the inflated stage to create contraction motion.^[26] By connecting the inflatable pouches in different configurations, other motion profiles such as pushing, bending, or twisting have also been demonstrated^[27] at the cost of losing the low-profile and planar design. Exploiting the pressure-induced axial extension mechanism (similar to IPAMs), Zhu et al.^[28] developed a class of fluidic fabric muscle sheets by inserting an array of elastic tubes inside wrinkled textile conduits. Upon pressurizing, these muscle sheets generated axial elongation due to the restriction from the textile structures that limit the radial expansion of the elastic tubes and only allow them to elongate axially. The fabric muscle sheets were reported to be capable of producing high forces and strains, and performing various motions such as elongation, bending, or shape changing (via the introduction of mechanical mismatch) with negligible tangential expansion.

There have also been studies employing fluidic actuators, both contracting^[29] and elongating,^[30] in the form of thin fibers or yarns to construct planar textile actuators directly. These yarns can be combined with themselves, other passive yarns, or textiles via several apparel techniques such as braiding, knitting, weaving, or sewing to form active structures that can perform motions and shape changes for a number of applications, including compression garments, shape-changing structures, bioinspired robots, and wearable haptic interfaces.^[30a,c,31] Although this approach has the advantage of a suitable form factor for incorporation with textile structures, the fabrication of planar textile actuators from these yarns can be complicated (i.e., due to their dissimilar mechanical properties with traditional yarns) and require dedicated machinery (e.g., knitting machines or weaving looms) and technical expertise from the textile industry. In addition, there is also a risk of potential degradation to these active yarns due to the high mechanical stress that they are exposed to during the fabrication process.^[10b]

On the contrary, the planar fluidic textile actuators described earlier can offer more facile fabrication processes based on reliable techniques such as laser cutting, thermal bonding, or computerized sewing, which can even result in a highly automated fabrication process (in the case of the multi-pouch PAMs). The planar design of these actuators also allows for the seamless incorporation of additional components (e.g., soft sensors or variable stiffness structures [VSSs]) to create advanced, multifunctional soft textile robotic systems.^[30b,32] Despite advantages, the multi-pouch PAMs still rely on pouch inflation for contraction, which may diminish the benefits of their planar design, and have limited contraction ratios (i.e., theoretical maximum ratio $\approx 36.3\%$ ^[26a,b]) while the design of fluidic fabric muscle sheets is currently limited by its manual insertion fabrication method.

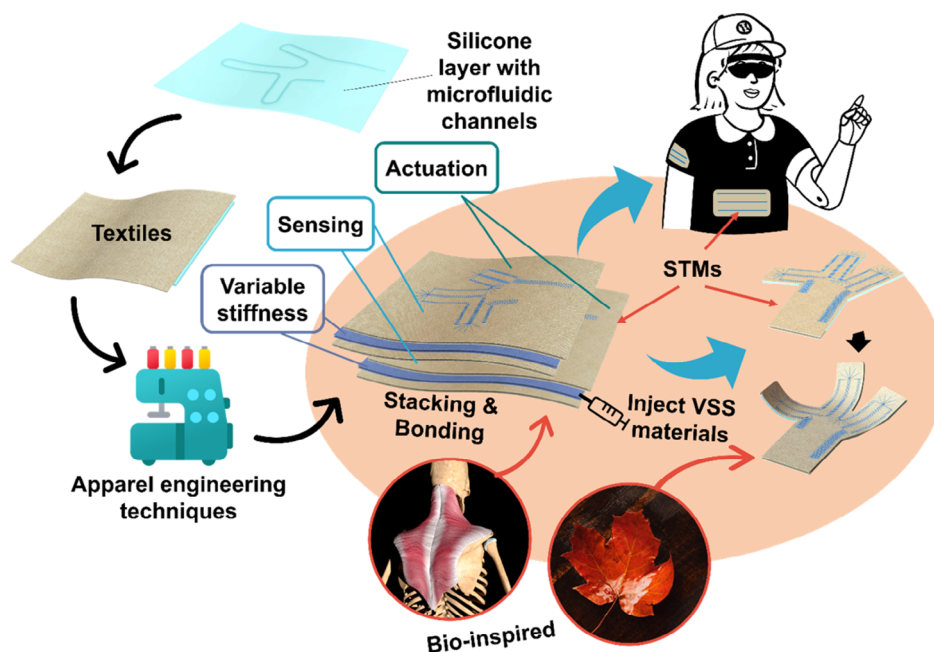


Figure 1. Illustration of the proposed soft textile muscles (STMs) that have a planar design (bioinspired by natural sheet-shaped actuators). Advantages of the approach include programmability by apparel engineering techniques, the ability to have multilayered structures via bonding (it is noted that the demonstration in this article is mainly a single layer of actuation, sensing, and VSS), and a high potential for large-scale and automated processes. Some prospective applications in soft robotic and wearable systems are also depicted.

Hereby, inspired by biological sheet-shaped actuators, this article introduces a new class of soft textile muscles (STMs) that have a planar design, programmability via apparel engineering techniques, and a fabrication method that has a high potential for being suitable for automated processes with scalable sizing. The new STMs build upon a multilayered silicone–textile composite structure consisting of fluidic channels embedded in silicone sheets, and employ textiles and sewn stitches for constraining and directing motions upon pressurization with fluid sources. The presented STMs are inherently compliant and highly conformable, and have a planar form factor which enables a facile integration of additional components (e.g., soft sensors, VSSs, or stretchable conductors) to potentially create advanced, multifunctional smart textile structures for robotic and wearable applications, as illustrated in **Figure 1**.

2. Results

2.1. Design Concept and Operation Principle of STMs

The new STM presented in this work is built on a silicone–textile composite structure comprising a silicone elastomer sheet sandwiched in between layers of textiles, as shown in **Figure 2A**. To generate motion, instead of using elastic tubes like prior research, the STMs employ programmable fluidic channels embedded in the silicone sheet as inflatable chambers, and textiles and stitches for circumferential constraints around the channels. Similar to other fluidic actuators, the STMs rely on fluid pressure, either compressible fluid (i.e., pneumatic) or incompressible fluid (i.e., hydraulic), to generate force and motion.

While compressible fluids (e.g., air or other gases) have the advantage of being light in weight and low in viscosity, their use often involves high noise, delays in response due to fluid compression, low efficiency, and requires more sophisticated control for loss compensation.^[33] On the contrary, hydraulic operations (e.g., water or oil) are advantageous with more rapid response, lower noise, and higher load capability at the cost of increased mass and viscosity.^[33] In this study, due to the aforementioned benefits, the STMs are operated with water as the hydraulic fluid. Additionally, the planar design of the proposed STMs also promotes a facile incorporation process of other silicone layers for additional functions (e.g., soft sensors for feedback information or a VSS for “move and hold” operations), as shown in **Figure 2A** and discussed later.

The working principle of the STMs is illustrated in **Figure 2B**. To provide hydraulic pressure to the STMs, syringes filled with water are connected to the fluidic channels of the STMs via fluid transmission tubes. By pushing or pulling on the plungers of syringes, either by hand or linear translational stages, water is pumped into or withdrawn from fluidic channels during the pressurization or depressurization stages respectively. As water is pumped into the fluidic channels, their internal pressure will increase and cause the channels to expand in all directions. However, due to the circumferential constraint imposed by textiles and stitches restricting the radial expansion of fluidic channels, the increased pressure can only produce an elongation of the STM structure along the longitudinal axis of its fluidic channels (**Figure 2B**—high pressure). This elongation also causes elastic energy to be stored in the silicone–textile structure. When water is removed (i.e., the internal pressure decreases

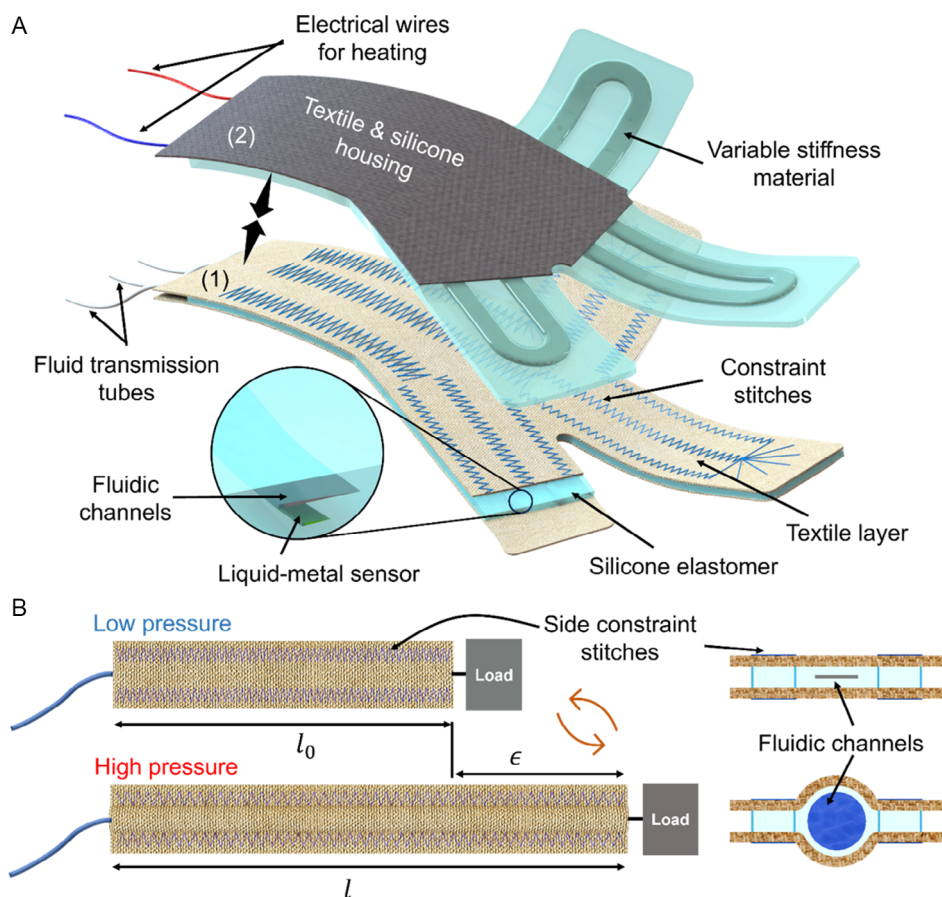


Figure 2. The design and working principle of the proposed STM. A) 1) A typical structure of an STM prototype based on fluidic channels embedded in a silicone sheet, and textiles and stitches for constraints. 2) The STM design can also integrate a soft sensor for feedback information and VSSs for stiffness tunability. B) Illustration of the working principle of the STM. The illustration is based on a single-channel STM with the side-zigzag stitch for constraining. Left: The STM elongates when internal hydraulic pressure increases (high pressure). When the pressure is removed (low pressure), the elastic energy stored in the STM is released and causes contraction. Right: The deformation of fluidic channels under low- and high-pressure conditions.

or depressurization, Figure 2B—low pressure), the stored elastic energy will be released and result in a contraction of the STMs. The range of force and elongation that can be produced depends on the dimensions of the STM prototypes, operating pressure range, and their constituent materials (i.e., types of silicone, textiles, and stitches). As a result, a simplified analytical model describing the effects of these factors is also implemented.

2.2. Fabrication and Actuation Capabilities

The fabrication of the STMs involves three main steps, including fabrication of the silicone sheet with desired embedded fluidic channels, constraining of the fabricated silicone sheet with textile and stitches, and installing and sealing of fluid transmission tubes for fluid supply (as illustrated in Figure 3A).

The fluidic channels embedded in silicone sheets in this study were fabricated by patterning very thin layers of liquid metals (LMs, such as EGaIn) on pre-fabricated silicone substrates. This fabrication method is developed based on an interesting property of LMs. Although bare LMs have the highest surface

tension of any liquid at room temperature ($>700 \text{ mN m}^{-1}$ ^[34]), which tends to keep them from sticking to other surfaces, their oxide layer (which is approximately 1–3 nm thick and can form almost instantaneously when the LMs are exposed to the atmosphere^[34]) has intrinsically strong adhesion to nonmetal materials, such as silicone elastomers.^[35] As a result, this adhesion can be utilized to reliably form LM patterns on silicone surfaces in the form of thin layers. When encapsulated by another layer of silicone elastomer, these thin LM patterns can separate the two silicone layers and form thin channels. These channels can allow fluids to pass through under pressure and serve as inflatable chambers for fluidic actuation. Other methods that can selectively separate silicone layers, such as using water-soluble tape^[36] or mold-release agents,^[37] can also be used for fabricating embedded fluidic channels in silicone sheets. However, LMs were employed for the fabrication of STMs in this study due to their better visualization of the fabricated channels, and the ease to pump fluids through these channels.

The use of LMs is also convenient for the fabrication of integrated soft piezoresistive sensors. LM patterns for fluidic channels can be fabricated by either stamping (Figure 3B) or

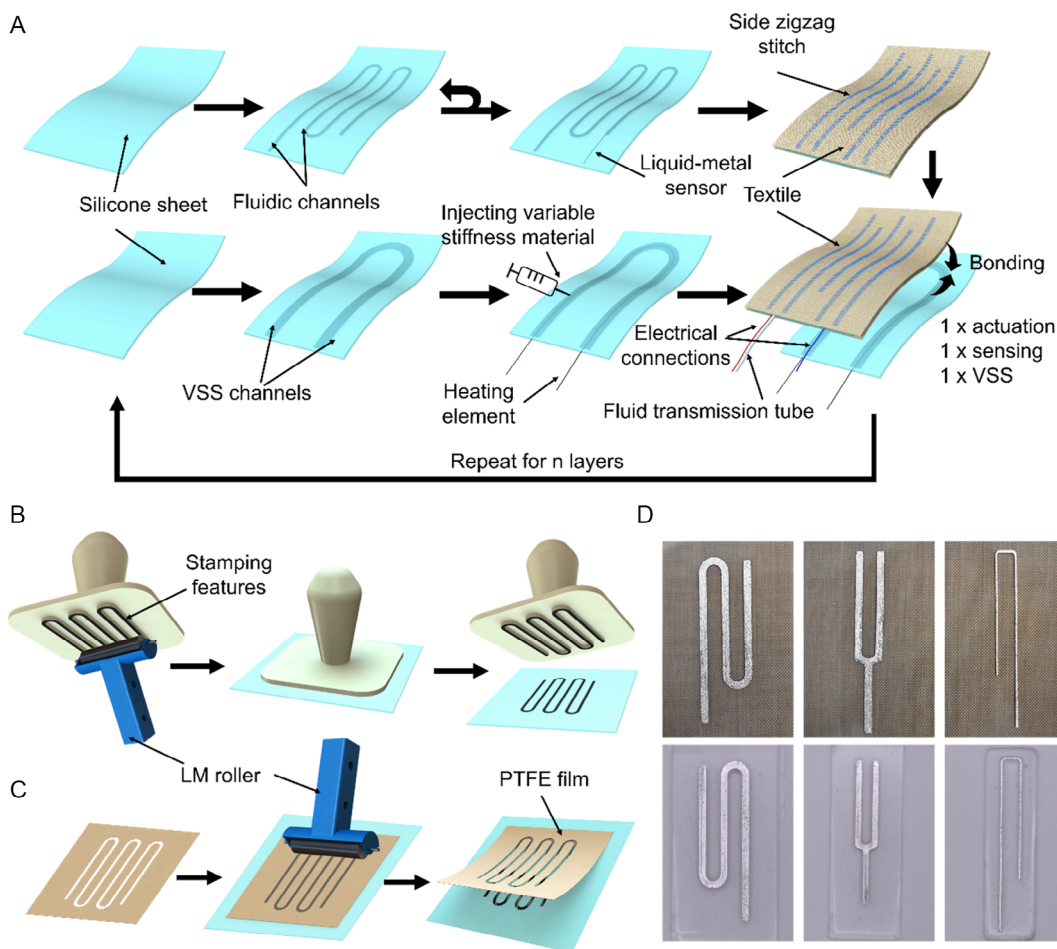


Figure 3. A) The fabrication process of the STMs involves three main steps, including fabricating fluidic channels embedded in the silicone sheet, constraining with textiles and stitches, and installing and sealing the fluid transmission tubes. The STMs can also be fabricated to incorporate liquid-metal soft sensing and VSSs. It is noted that this illustration is for fabrication process of one layer of each function and other designs that employ multiple layers can be achieved by repeating this process. Illustration of the B) stamping and C) stencil-printing methods to create LM patterns for fluidic channels. D) Examples of LM patterns fabricated by the stamping method (top) and the corresponding stamps (bottom). The designed width values of the stamping features are as follows: left: 2 mm; middle: 2 mm; and right: 0.5 mm.

stencil-printing (Figure 3C) methods. While the stencil-printing method allows for the rapid fabrication of different fluidic channel designs, the stamping method is more suitable for mass production, where a stamp for a channel design can be created and used to manufacture a number of prototypes. Figure 3D displays the LM patterns for several fluidic channel designs fabricated by the stamping method, with a stamping feature as small as ≈ 0.5 mm being successfully created.

Once the embedded fluidic channels had been successfully fabricated, textiles were bonded to the silicone sheets on both top and bottom surfaces, and stitches were directly sewn over the silicone–textile composite structure to provide circumferential constraint around the channels. There are different sewing methods that can be used for this purpose. When the prototypes can fit the embroidery hoop, computerized embroidery is the best option for accuracy and speed at the expense of extra work for alignment. Machine sewing is another good option, where constraining stitches are sewn with manual movement of the

STM prototypes under the sewing foot of a sewing machine. This method can provide good accuracy and strong stitches, and can accommodate large prototypes. After the STMs were constrained with textiles and stitches, fluid transmission tubes made from polytetrafluoroethylene (PTFE) tubing were connected to the fluidic channels for fluid supply. The connection between fluid transmission tubes and STMs was then reinforced by knots of polyester threads and superglue for a watertight seal. After fabrication, the STMs need to be actuated for a few cycles to stabilize the mechanical response before their first usage. It is noted that by having the fluidic channels embedded in the silicone sheets and directly constrained by textiles and stitches (instead of the manual insertion of elastic bladders/tubes into textile structures), the design and fabrication method for the STMs presented in this study can theoretically have any desired channel designs to be fabricated while exhibiting a high potential to adopt more automation into the manufacturing process (as illustrated in Figure 1).

Operating on the stored elastic energy of the constituent materials and fluid pressure, the STMs have their performance (e.g., force or elongation) greatly dependent on the selection of silicone elastomers, textiles, and stitching patterns. Because the textiles' structure cannot be further modified (e.g., induce wrinkling) after the silicone–textile composites are fabricated, STMs need to make use of stretchable textiles, which can be either uniaxially (i.e., one-way) or biaxially (i.e., two-way) stretchable, and zigzag stitches to preserve the textile stretchability (because the normal straight stitch is inextensible). When biaxially stretchable textiles are used, a cross-zigzag stitch (i.e., the stitch goes over and around the fluidic channels, **Figure 4B,C**) is preferred to minimize the undesired radial expansion of the fluidic channels under hydraulic pressure. In contrast, if the uniaxially stretchable textiles are used, either cross- or side-zigzag stitches can be employed to constrain the fluidic channels, although the cross-zigzag stitch is also known for not accommodating as high

an elongation as the side one.^[28] This limitation can probably be attributed to the fact that the cross-zigzag stitch may put more constraints on the fluidic channels and textile layers during elongation. As a result, to maximize the elongation of the STMs while minimizing the radial expansion, the use of uniaxially stretchable textiles and side-zigzag stitch is optimal.

In the meanwhile, the cross-zigzag stitch is also effective for other types of motion that do not require as much elongation (**Figure 4B,C**), with the benefit of fewer sewing steps required to constrain fluidic channels. Normally, the stretchability of textiles and stitches (i.e., without wrinkling) is much smaller than that of silicone elastomers (around 100% strain compared with several hundred percent).^[10b,38] As a result, the stretchability of the STMs in this study within the operating pressure range is mainly limited by the constituent textiles and stitches. By changing the configurations (i.e., different channel designs) and compositions (e.g., the introduction of non-stretchable textiles), the

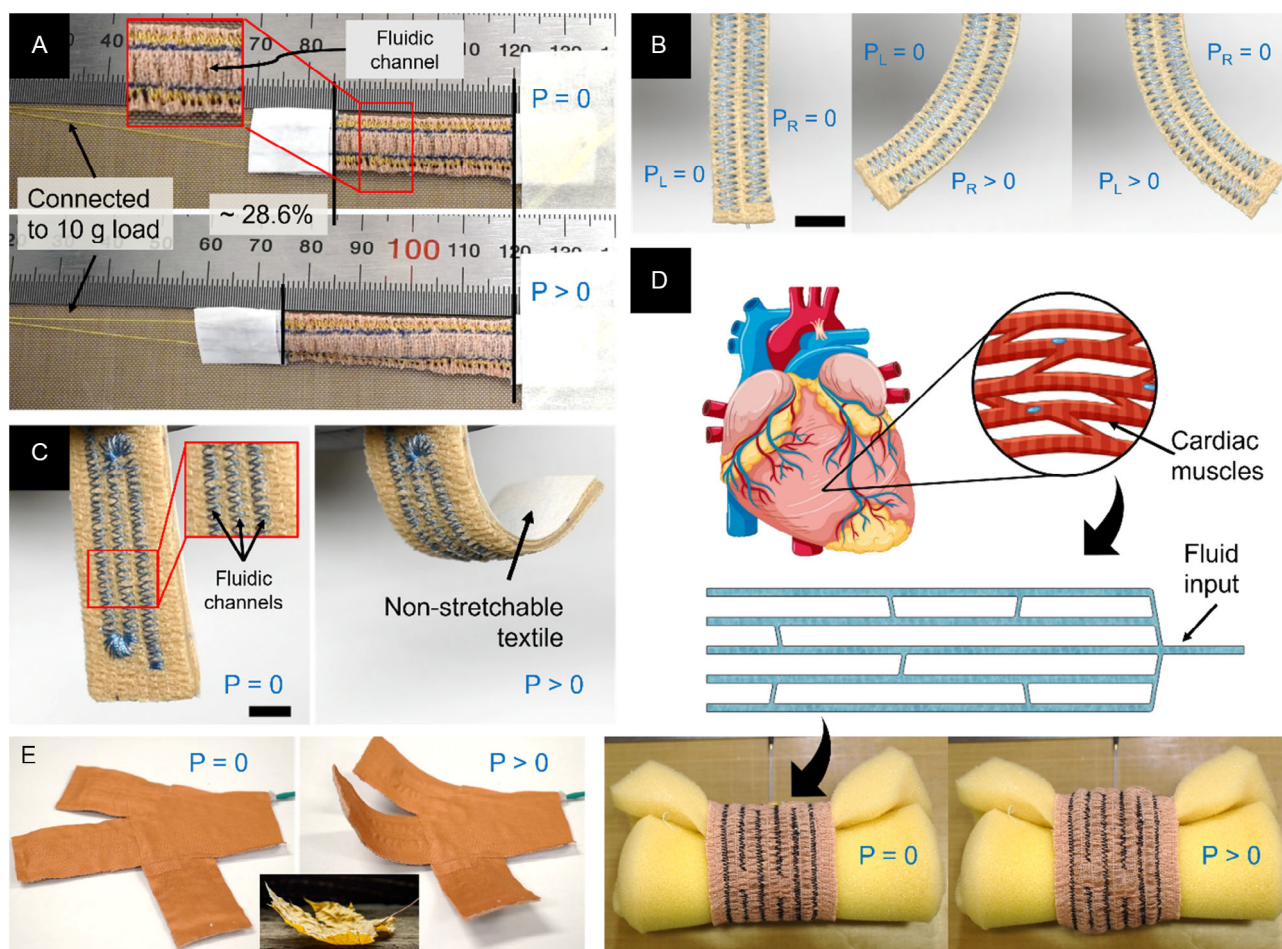


Figure 4. Representative STM prototypes with uniaxially stretchable textiles and zigzag stitches. A) An STM prototype performing elongation under hydraulic pressure. The inset shows the yellow side-zigzag stitch with a fluidic channel in the middle. B) An STM prototype with two fluidic channels controlled separately performing bidirectional bending. C) An STM prototype performing out-of-plane bending. The inset shows the blue cross-zigzag stitches over the fluidic channels. Scale bars—10 mm. D) An STM sheet with a channel design inspired by the human cardiac muscle. When rolled into a band, the STM sheet can expand under hydraulic pressure and apply compression when the pressure is removed (the heart and cardiac muscle images are designed by brgfx/Freepik.com). E) An STM prototype with a multidirectional channel design in a single sheet (**Figure S1E**, Supporting Information). Under hydraulic pressure from a single input, three fingers pointing in three different directions can bend simultaneously, forming a shape similar to the dry maple leaf in the inset.

STMs can also be programmed to perform a variety of motions, as demonstrated in Figure 4, S1 and Video, Supporting Information.

2.3. Characterization of the STMs

As our experiments demonstrate, STMs can be programmed to perform a variety of motions, the fundamental one of which is axial elongation under hydraulic pressure. To characterize the presented STMs, an experiment was conducted to evaluate the mechanical behaviors of the single-channel STM prototypes (with uniaxially stretchable textile and side-zigzag stitch, Figure S1A, Supporting Information) with respect to the input hydraulic pressure and volume. The experimental setup for the characterization is displayed in Figure S2, Supporting Information, and described in Experimental Section. Figure 5A shows the relationship between the output elongation of an STM prototype and the input hydraulic pressure and volume. The experimental results reveal that the STM prototype (31 mm active length and 2 mm fluid channel) could reach

approximately 64.7% elongation with about 1.1 mL (milliliter) of input volume, which corresponds to approximately 121.3 kPa of pressure. It can also be observed that the relationship between the input volume and the STM's elongation is highly linear with little hysteresis between the pressurizing and depressurizing phases, which reflects the incompressibility of the hydraulic medium. To the contrary, the pressure–elongation relationship of the STM exhibits a larger hysteresis profile, displayed as a larger gap between the pressurizing and depressurizing phases, which can be attributed to the nonlinearity of hyperelastic materials at large deformations.

Figure 5B displays the contraction force generated by an STM prototype (33 mm active length and 2 mm fluid channel) in response to the input pressure and volume. The experimental results show that the contraction force increased with the decrease in fluid volume and pressure, which has been described in the operation principle of the STMs above. As water is removed from fluidic channels, the internal pressure will decrease, causing the elastic energy stored in the STMs during the pressurization stage to be released and result in contraction

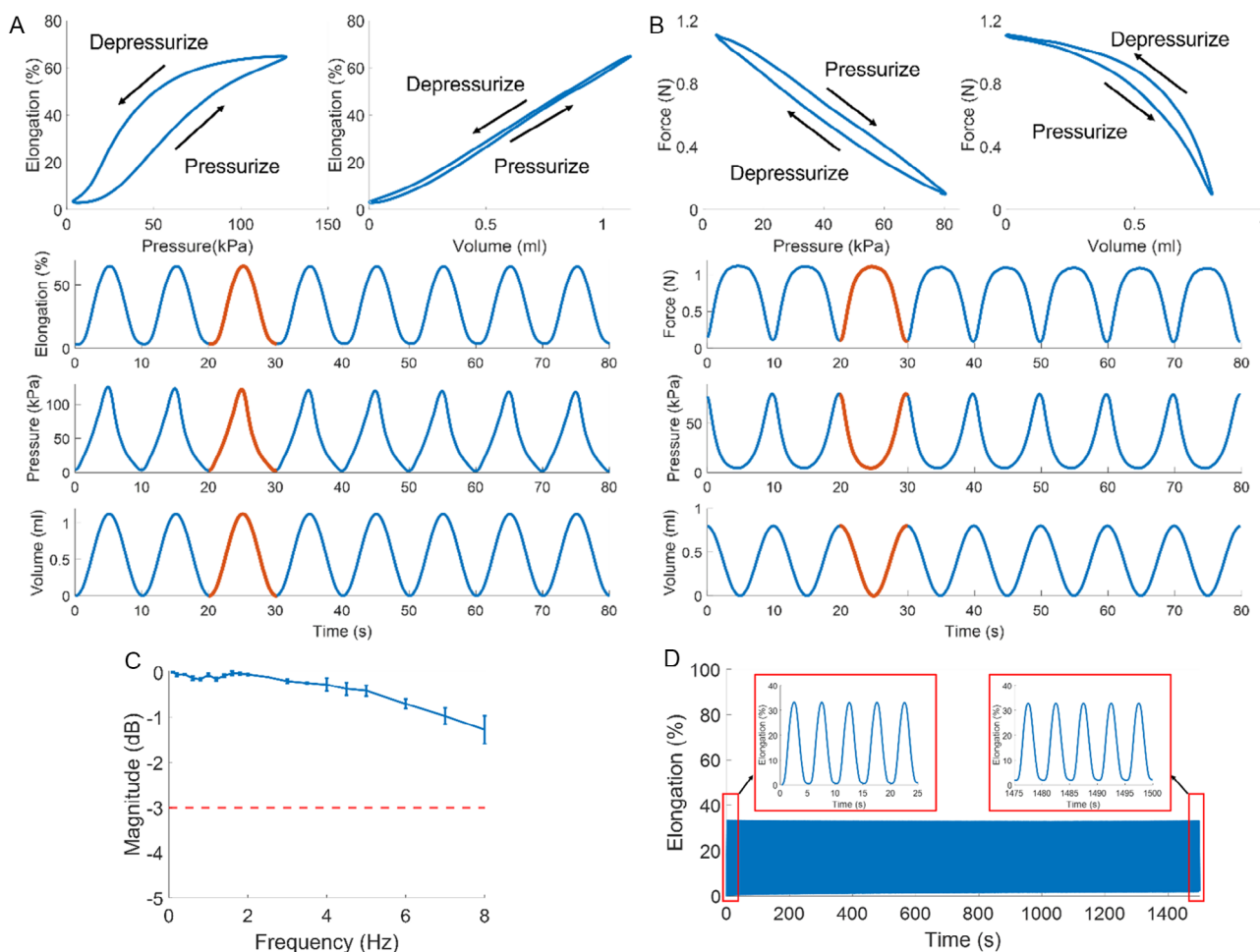


Figure 5. Mechanical characterization of the single-channel STM prototypes with uniaxially stretchable textile and side-zigzag stitch constraint. A) Elongation and B) force responses of the STM prototypes with respect to input volume and hydraulic pressure. C) The frequency response of the STM prototype actuated at approximately 10% elongation. The error bars represent one standard deviation. $N=3$ measurements. D) Repetitive response of the STM prototype during the durability test of 300 cycles.

of the STMs. When pressurized to approximately 62.1% elongation and depressurized to contract, the tested STM prototype could generate a force of approximately 1.1 N with a moderate hysteresis profile being observable in its pressure–force relationship, which can be attributed to the hyperelastic materials and the friction during the experiment. Figure 5C shows the frequency response of the STM prototype when being actuated to approximately 10% elongation with driving signals of various frequencies from 0.1 to 8 Hz. Its frequency response was then evaluated via the reduction in the STM prototype's elongation at each frequency compared to the first one by the root-power quantity equation: $M(f) = 20\log(A_f/A_0)$, where $M(f)$, A_f , and A_0 denote signal magnitude (dB), STM's displacement (in mm) at frequency f , and STM's elongation at the first frequency (0.1 Hz), respectively. The results show a decrease in the STM's elongation when the input frequency increases, with the STM prototype losing its elongation by approximately 13.6% (−1.27 dB) at 8 Hz. However, these values are still far from the typical −3 dB cutoff frequency, indicating that the STMs presented in this study are able to operate effectively at frequencies of at least 8 Hz, which can cover a wide range of soft robotic and wearable applications.^[10b] The durability and repeatability of the STMs were also characterized and demonstrated in Figure 5D, where an STM prototype was pressurized to elongate to over 30% elongation for 300 cycles. The results display a relatively robust operation of the STM prototype over cyclic actuation, with shrinkage in elongation being about 5.7% after 300 cycles, which can be attributed to the viscoelastic behavior of the materials.

2.4. Analytical Model

To study the pressure-induced axial elongation of the STMs, a simplified analytical model was also developed in this study with several assumptions. First of all, the fluid used for the STMs follows quasi-hydrostatic behavior, which means that the STMs slowly elongate under hydraulic pressure. As a result, the fluid's inertial force is small and can be neglected. Second, as textiles and silicone sheets are bonded together, they should move with the same displacement, and therefore, the friction between them should be negligible. Additionally, the Poisson's ratio of the silicone is assumed to be 0.5, which means that its material volume should stay constant during deformation.

In this section, the simplified analytical model was developed based on the STM prototype fabricated with uniaxially stretchable textile and side-zigzag stitch. It is hypothesized that the axial elongation of STMs happens in two phases, as illustrated in Figure 6A. Initially, the STM is fabricated with an initial length l_0 and a cross-sectional area $A_0 = A_{s0} + A_{f0}$, where A_{s0} and A_{f0} are the initial cross-sectional areas of the silicone sheet and the fluidic channel. It is noted that the A_{s0} is the total area of all silicone cross sections, including the area between the two side stitches (i.e., active area, A_{s0_active}) and the two silicone areas on the sides ($A_{s0_passive}$). Upon pressurization, the STM is hypothesized to enter the first phase of deformation where its active area (i.e., the area constrained between side stitches) changes the cross-sectional shape, expanding radially from a rectangular cross section to a relatively circular one, with negligible elongation (Figure 6A—Phase 1). During this phase, it was also

observed that the width of the active area (i.e., the distance between two constraining stitches) experienced negligible changes, and therefore, it can be assumed that the cross section of the active area changes from a rectangular shape with a width w into a circular one with equal diameter, $d = w$. The reason for this deformation may be attributed to the fact that although the constraining textile was uniaxially stretchable, there are still some movements between textile yarns along the non-stretchable direction (Figure S3, Supporting Information) and between the textile layers and the constraining stitches, which allows for some degree of radial expansion when the STM is pressurized. When the hydraulic pressure continues to increase, the cross-sectional change stops, and the STM starts to elongate only in the second phase (as illustrated in Figure 6A—Phase 2). With the assumptions mentioned earlier, the force production F_{net} of the STM during axial elongation can be generally modeled as

$$F_{net} = F_s + F_{tx} - F_f \quad (1)$$

where F_s and F_{tx} are the elastic forces produced due to the stretching of the silicone and textile layers, respectively, and F_f is the axial force induced by the hydraulic pressure, P . Assuming that the STM operates in a linear elastic regime with elastic modulus, E , and elongation, ϵ , the force produced by the STM can be written as

$$F_{net} = E_s A_s \epsilon + E_{tx} A_{tx} \epsilon - N P A_f \quad (2)$$

where N is the number of fluidic channels embedded in the silicone sheet, A is the cross-sectional area of each layer, and P is the applied hydraulic pressure. Under the third assumption, in which the volume of the silicone stays constant through all phases (Figure 6A), we have

$$A_{s0} l_0 = A_{s1} l_1 = A_{s2} l_2 \quad (3)$$

Because it is assumed that the elongation during the first phase is negligible, we can have $l_1 = l_0$, and therefore, $A_{s1} = A_{s0}$. As a result, Equation (3) can then be rewritten as

$$A_{s2} = \frac{A_{s1} l_1}{l_2} = \frac{A_{s1}}{1 + \epsilon} = \frac{A_{s0}}{1 + \epsilon} \quad (4)$$

And Equation (2) becomes

$$F_{net} = E_s A_{s1} \epsilon + E_{tx} A_{tx} \epsilon - P (A_2 - A_{s2}) \quad (5)$$

Because it is assumed that there is no cross-sectional change during the second phase, we can also have $A_2 = A_1$. Upon pressurization at a certain hydraulic pressure P , the STM can yield an elongation, ϵ , with $F_{net} = 0$, and therefore, the relationship between the STM's elongation and input hydraulic pressure can be expressed as

$$P = \frac{(E_s A_{s1} + E_{tx} A_{tx}) \epsilon^2 + (E_s A_{s1} + E_{tx} A_{tx}) \epsilon}{A_1 \epsilon + A_1 - A_{s1}} \quad (6)$$

The results of the simplified analytical model were compared with the characterization results in Figure 6B,C for two STM prototypes, including a single-channel prototype and a double-channel prototype (Figure S1A,B, Supporting Information). The input parameters for the model are listed in Table S1, Supporting Information. As demonstrated, despite being simple,

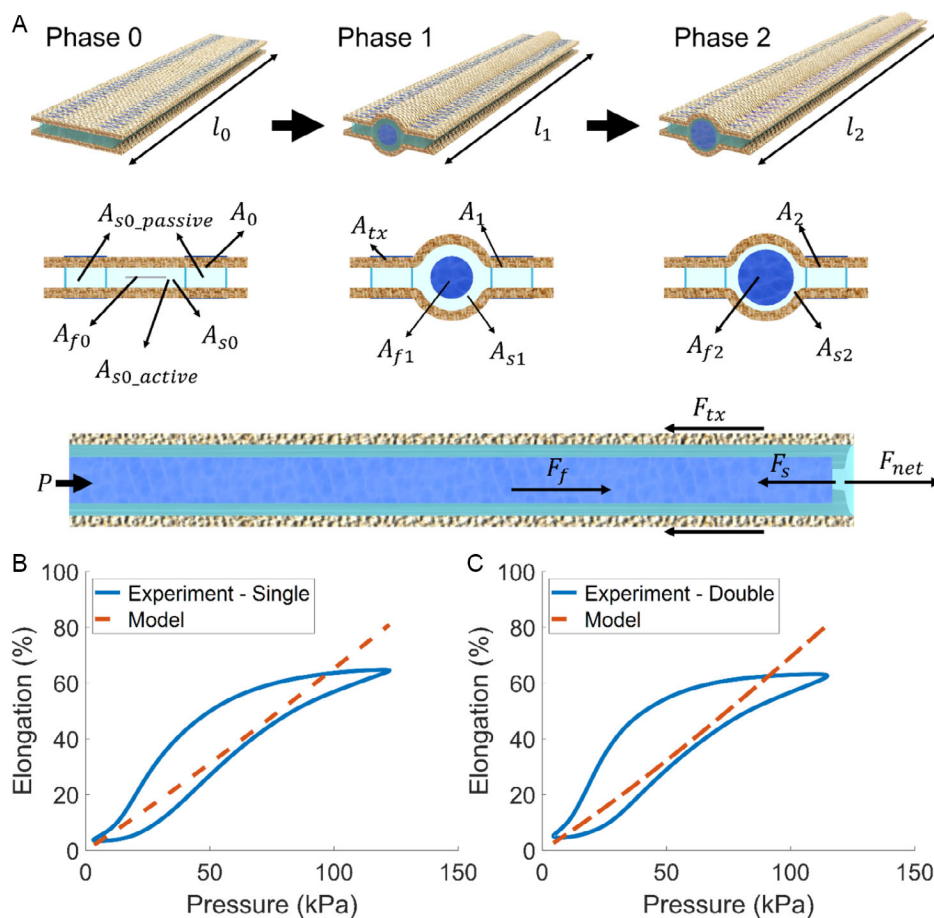


Figure 6. Analytical model for the axial elongation of the STM under hydraulic pressure. A) Deformation and force diagram of a single-channel STM during axial elongation with two phases, including cross-sectional change with negligible elongation during the first phase and elongation only during the second phase. B) Comparison between the analytical model and the experimental elongation of a single-channel STM prototype. C) Comparison between the analytical model and the experimental elongation of a double-channel STM prototype.

the analytical model developed in this section can provide a good description of the nonlinear relationship between the elongation of the STM prototypes and input hydraulic pressure. However, there is still a deviation between the model and the experimental data, particularly at the high elongation end, which can be attributed to several factors, such as the hyperelastic characteristics of both the silicone and textile used to construct the STM prototypes (Figure S3, Supporting Information) and the frictional losses that are not taken into account in the model.

In addition, another possible reason for the deviation in the analytical model can be attributed to the assumption that the STM undergoes two phases during axial elongation, which actually can happen simultaneously under hydraulic pressure, which requires a more complicated model to describe. Additionally, there also exists a hysteresis in the response of the STMs that can be due to the viscoelasticity of the constituent materials that our model did not take into consideration.

2.5. Integrated Piezoresistive Sensor

Sensing is an important part of any soft robot to detect internal or external changes and respond appropriately. Thanks to the

fabrication method based on LM patterns by 2D fabrication techniques, the STMs proposed in this study can also incorporate soft piezoresistive sensors in their structures that can be used to provide feedback information of either STMs' status (e.g., elongation or bending curvature in closed-loop control) or external stimuli (e.g., external pressure, or stretching that can be useful as user inputs in wearable and interactive applications). For illustration, a representative STM prototype with a double-layer structure is shown in **Figure 7A**, where one layer of the prototype was used for actuation and another layer contained an integrated piezoresistive sensor. This piezoresistive sensor can be created by employing the same LM used for the fabrication of the STMs, which further simplifies the fabrication process. The sensor can be embedded in the same silicone sheet with the fluidic channels and together constrained by textiles and stitches. This design not only results in a thin, monolithic structure of actuator and sensor but also helps enhance the sensitivity of the sensor to pressure-induced elongation of the STMs due to the synergistic effect from both elongation and radial expansion of the fluidic channels acting on the sensor under hydraulic pressure. The mechanism for this enhancement is illustrated in **Figure 7B**.

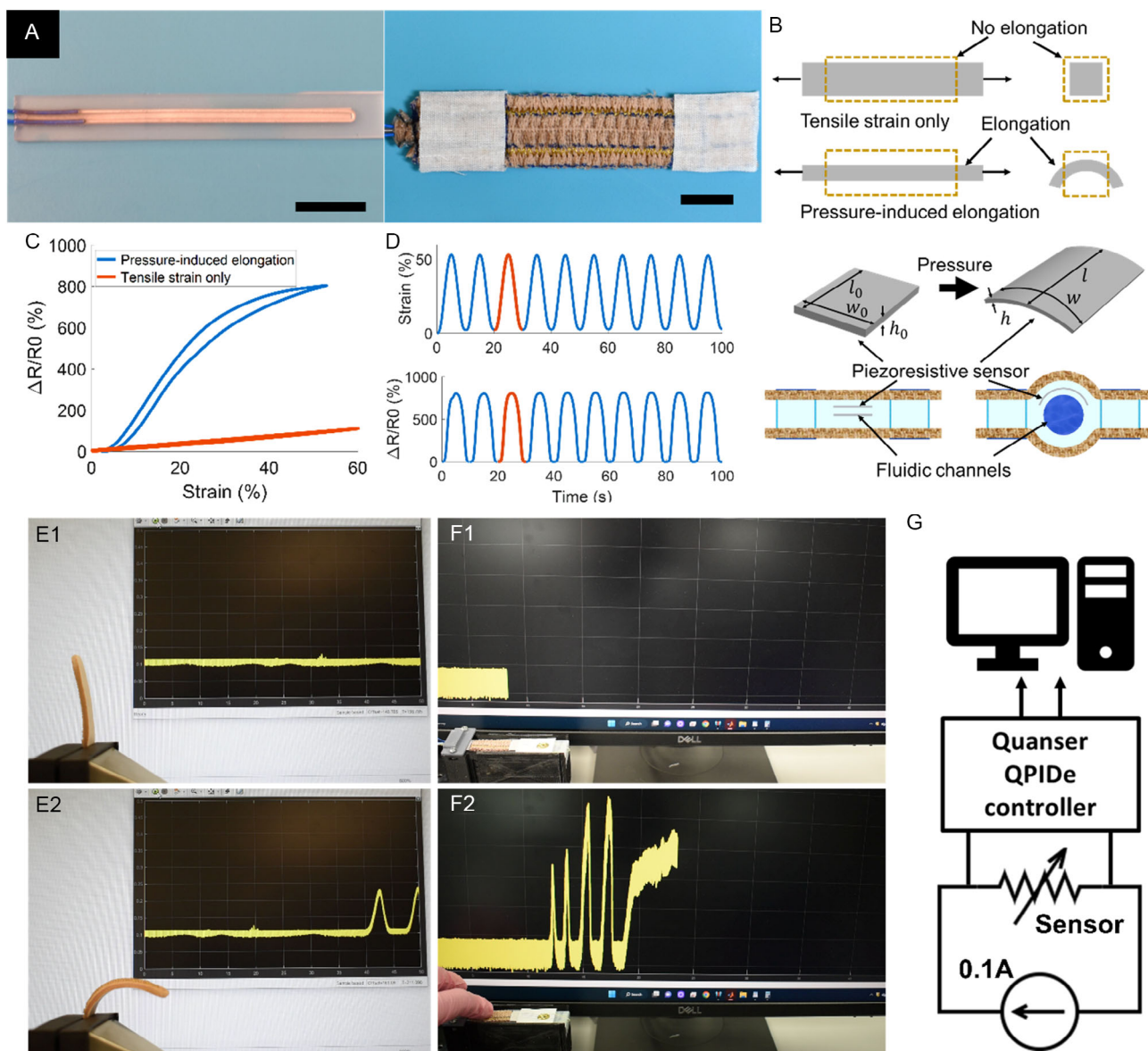


Figure 7. STMs with integrated piezoresistive sensors. A) A representative double-layer STM prototype with one layer for actuation and one layer containing a soft piezoresistive sensor made from LM. Scale bars—10 mm. B) An illustration of the mechanism for enhanced sensitivity of the piezoresistive sensor to pressure-induced elongation of the STMs. C) A comparison in resistance changes, $\Delta R/R_0$, of the sensor when it is under pressure-induced elongation and when it is subjected to tensile strain only. D) Repetitive response of the piezoresistive sensor during pressure-induced elongation. Demonstration of the potential use of the integrated piezoresistive sensor for monitoring E) STMs' bending motion and F) applied external pressure. E1,F1) The sensor's signal at initial stage. E2,F2) The sensor's signal during STMs' bending motion and applied external pressure, respectively. G) A schematic diagram of the readout circuit for recording the piezoresistive sensor's signal.

The resistance of the piezoresistive sensor is defined as $R_0 = \rho l_0/A_0$, where ρ is the resistivity of the LM, l_0 is the length, and A_0 is the cross-sectional area of the conducting pathway. Upon deformation (e.g., elongation or external compression), the resistance of the piezoresistive sensor will change according to changes in the geometry of the conducting pathway. For example, when subjected to tensile strain, the piezoresistive sensor will undergo an increase in length (l) and a reduction in cross-sectional area (A) (as shown in Figure 7B), which causes its resistance to increase. However, when the piezoresistive sensor functions to sense the

pressure-induced elongation of the STMs, due to being embedded close to the fluidic channels and constrained by textile and stitches, the sensor will not only experience an increase in length and a reduction in cross-sectional area due to elongation, but the radial expansion of the fluidic channels also applies additional compression on its conducting pathway. This additional compression further deforms the sensor's cross section (from a rectangular shape to a C shape, as shown in Figure 7B) and reduces its cross-sectional area, which helps improve the sensitivity of the sensor to pressure-induced elongation.

Experimental characterization displayed in Figure 7C shows the resistance change ($\Delta R/R_0$) of the piezoresistive sensor when the double-layer STM prototype was elongating under hydraulic pressure in comparison with the resistance change of the same sensor when it was subjected to tensile strain only. A significant enhancement in the sensitivity of the integrated piezoresistive sensor to pressure-induced elongation of the STM prototype can be observed with a small hysteresis ($\Delta R/R_0 \approx 800\%$ at 50% elongation compared to $\Delta R/R_0 \approx 100\%$ of the same sensor but experiencing tensile strain only). The repeatability in resistance changes of the piezoresistive sensor during pressure-induced elongation was also demonstrated in Figure 7D. Figure 7E,F demonstrates the potential use of the integrated piezoresistive sensor for monitoring the STMs' bending motion and applied external pressure (Video, Supporting Information).

2.6. VSSs

Due to their inherent compliance, soft robots are usually ill-suited for load-bearing applications. Therefore, VSSs, which can exhibit an on-demand change in stiffness, can be a useful additional component for soft robots in applications where load-bearing capability or “move and hold” operations are required. In addition, integrating VSSs into wearable devices can also provide adaptable anchoring points and improve the conformability of the devices to the complex geometry of the human body. The STMs presented in this study can also facilitate

incorporate thermo-responsive VSSs in their structures for these purposes. There have been a number of methods to create thermo-responsive VSSs,^[39] among which the injection method where variable stiffness materials are injected into tubes or pre-formed channels/molds has the benefit of achieving VSSs of complex and diverse shapes and sizes. However, to be injectable, variable stiffness materials should be able to temporarily stay in the liquid state with a moderate viscosity. As a result, this fabrication method is normally employed for only either low-melting-point alloys (LMPAs)^[40] or thermo-responsive epoxy (e.g., EPON 828 and Jeffamine D400^[13]), which were both demonstrated usable for the development of VSSs in this study (Figure 8). In Figure 8A, a multidirectional bending STM prototype equipped with a VSS made from an LMPA (melting point at approximately 47 °C) was demonstrated in a load-bearing operation. The VSS was fabricated by injecting the liquid LMPA into channels formed by the same channel fabrication method presented earlier. During the experiment, the VSS was heated until soft via Joule heating with an enameled metal wire running through the LMPA channels, and the STM prototype was pressurized to bend its fingers. A load of 200 g was then placed on top of the bending prototype under two scenarios: 1) while the STM prototype was pressurized and the VSS was soft (top row—Figure 8A), and 2) while the STM prototype was pressurized and the VSS was let cool and stiffen (bottom row—Figure 8A). It can be observed that the bending finger in the bottom row is more upright than the one in the top row, indicating that the bending prototype in the bottom row did not experience

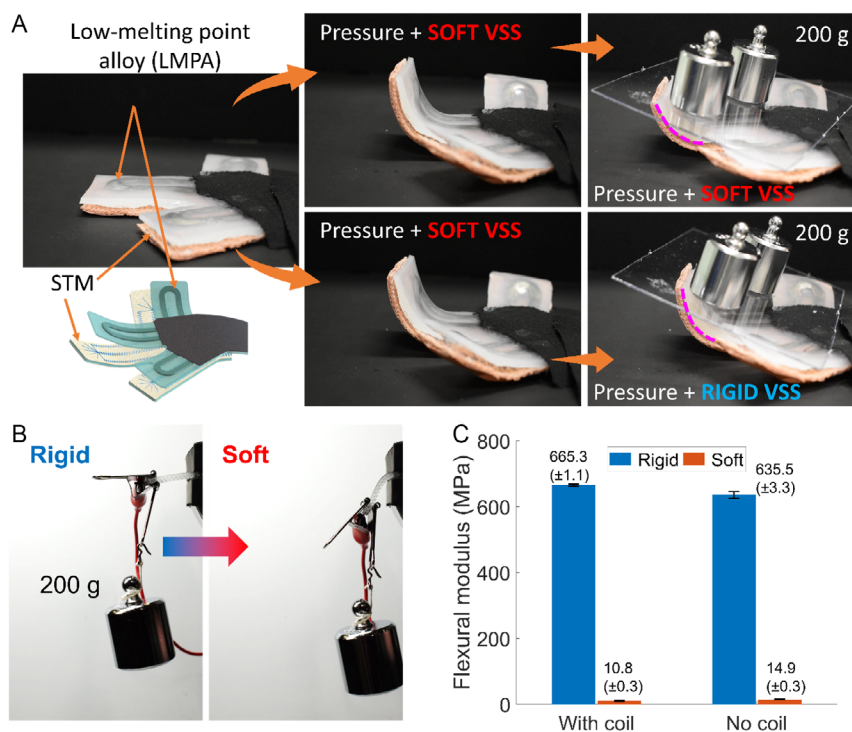


Figure 8. Variable stiffness structures (VSSs) for the STMs. A) A multidirectional bending STM prototype equipped with an LMPA-based VSS in a load-bearing operation. The dashed pink lines highlight the deformation of the bending fingers under loading condition in two cases. B) Demonstration of the transition from the rigid state to the soft state of a VSS prototype based on 832WC thermo-responsive epoxy. C) Flexural moduli of the 832WC thermo-responsive epoxy during rigid and soft states with and without the heating coil. The error bars represent three standard deviations because one standard deviation is too small to be visible in the graph. N = 3 measurements.

as much deformation as the one in the top row under the same load. This result shows the contribution of the additional VSS in enhancing the load-bearing capability of the bending STM prototype (Video, Supporting Information).

In addition to using LMPA, thermo-responsive epoxy could also be used for the VSSs in this study, as shown in Figure 8B. Although VSSs based on thermo-responsive epoxy, EPON 828 and Jeffamine D400, have been reported in several studies,^[10a,41] EPON 828 has a relatively high viscosity (about 110 000–150 000 cP^[42]), which can make the fabrication process challenging. In this study, a new thermo-responsive epoxy (832WC, MG Chemicals) was investigated for the VSSs due to its very low viscosity of only 980 cP, which can be more suitable for the injection method, and low glass transition temperature (approximately 33 °C^[43]), which can potentially reduce energy consumption, shorten heating and cooling time, and be beneficial for wearable applications. Under thermal stimulation, the VSSs based on the 832WC thermo-responsive epoxy can soften when the epoxy undergoes a transition from the glassy state (i.e., rigid) to the rubbery state (i.e., soft). As shown in Figure 8B, a VSS prototype based on the 832WC epoxy was stiff enough to withstand a 200 g weight at its glassy state but quickly became soft and bent down under the load of the weight after being heated. Instead of using metal wires, miniature metal coils could also be employed to provide Joule heating to the VSSs. This design can not only allow the heating energy to spread rapidly through the material to speed up the softening process of the VSSs but also can enable the creation of an inner hollow channel for active cooling (e.g., using cold air or water) to increase the speed of the stiffening cycle, which has long been a challenge of thermo-responsive VSSs. There can be several methods to fabricate hollow channels inside the heating coils, such as inserting silicone tubes, wax filaments, or water-soluble filaments (depending on applications) inside the coils before injecting the thermo-responsive epoxy and removing them once the epoxy is cured. Figure S5A, Supporting Information, shows the fabrication of VSSs of different curvatures based on the 832WC thermo-responsive epoxy injected into preformed channels and metal coils with inner hollow channels shown in the inset. The stiffness variation between the rigid and soft states of the 832WC epoxy was also characterized and is presented in Figure 8C. The characterization results reveal a stiffness variation ratio of about 42.7–61.6 times when the epoxy was heated up to approximately 50–55 °C from room temperature. It is also shown that there is not much difference in flexural moduli between the 832WC VSS prototype containing the heating metal coil and the prototype without the coil for both rigid and soft states. This result indicates the negligible contribution of the metal coils to the stiffness of the VSSs, particularly during the soft state, due to the coils' high flexibility.

It is noted that unlike the LMPAs, which require custom channels for liquid containment, the thermo-responsive epoxy can be fabricated as stand-alone VSSs thanks to their transition between the glassy and rubbery states. As a result, the 832WC epoxy in this study can also be employed for the fabrication of stand-alone VSS prototypes, as shown in Figure S5B,C, Supporting Information. After fabrication, the 832WC stand-alone VSS prototypes could also be combined with textile substrates for seamless integration with STMs and STM-based textile robotic

systems. The textile substrates can also provide an extra insulation layer to help lower the surface temperature of the stand-alone VSSs, which can be beneficial in wearable devices. Figure S5C, Supporting Information, displays the difference in surface temperature between the bare area and the area covered by textile substrates of an 832WC stand-alone VSS prototype, showing that while the VSS prototype was heated to 50.2 °C, the surface temperature on the textile substrates was only 38.2 °C, which is 12 °C lower than that of the prototype and not much hotter than the body temperature.

2.7. Application

Skin-stretch (SS) haptic feedback is a well-known physiological apparatus for human haptics or the sense of touch, playing a significant role in our way of interacting with the surrounding environment. Recently, it has also been shown to be a useful indicator in guiding human motion, or rendering friction, objects' stiffness, or surface geometries,^[44] which can be of great benefit for emerging applications in motion guidance and navigational assistance, remote surgical systems, rehabilitation, training, entertainment, or virtual reality (VR) and augmented reality (AR) (Figure 9A). As a result, several studies have been conducted to recreate the SS haptic feedback by applying shear force on the skin via a tactor in the form of compact, wearable devices.^[6a,45] To enhance the wearers' comfort, there has been a shift in SS haptic devices from using rigid components (e.g., cables, DC motors, and plastic housing) to softer counterparts (e.g., soft artificial muscles and soft materials for housing). Thanks to being entirely made of soft materials (e.g., silicone elastomers and textiles), the STMs presented in this study can be a particularly suitable candidate for fabricating wearable devices. As a result, a completely soft, 3D SS haptic device based on the STMs is demonstrated later as an example application of the STMs in this work.

While most of the SS haptic devices were targeted for fingertip wearing, which normally limits the size of the device and potentially imposes interferences with concurrent interactions between the hands and physical objects, there are other regions of the body (e.g., arms, legs, wrists, chests, or back) that can also be effectively used for haptic feedback without interfering with the interactions of the users' hands and fingers.^[46] As a result, the 3D SS haptic device demonstrated here was also developed for those areas of the body rather than the fingertips. Figure 9B provides an overview of the architecture of a representative 3D SS haptic device, which consists of a top cover made of textiles, and a main 3D SS device powered by four STMs and a silicone balloon. A soft tactor made from TPU was attached on the other side of the SS device, opposite to the silicone balloon, as shown in Figure 9B–II. Upon pressurization, this silicone balloon will inflate and compress the soft tactor against the skin, generating a normal force on the skin's surface. Meanwhile, under hydraulic pressurization, the four STMs will elongate and drag the soft tactor across the skin's surface, inducing shear forces and a stretch sensation to the skin. As the four-STM sheet was designed and fabricated from a single silicone–textile composite structure, the SS device in this work is a monolithic and completely soft, textile-based wearable device that can be worn on various locations of

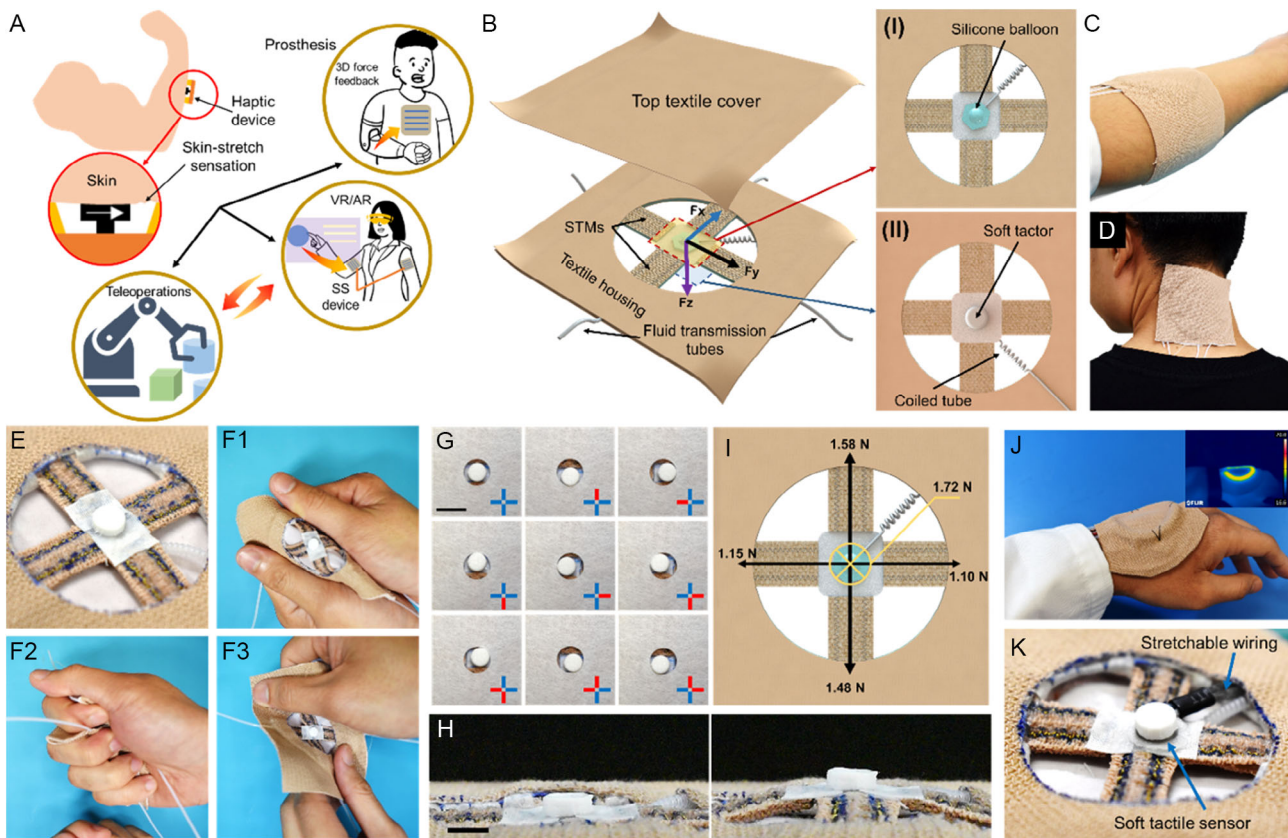


Figure 9. The wearable, STM-based 3D skin-stretch haptic device. A) The working principle of skin-stretch haptic devices and their potential applications in providing haptic feedback for prosthesis, in VR/AR environment and teleoperations. B) Exploded view schematic illustration of the 3D skin-stretch device. I) Top view of the device shows the silicone balloon for normal force generation. II) Bottom view of the device shows the soft factor. Images of the 3D skin-stretch device conformably worn on different locations of the body, including C) the user's arm and D) the user's neck during rotation. E) A closeup bottom view of the skin-stretch device showing the soft factor and the four STMs. F1–3) The 3D skin-stretch device is highly flexible and soft, which can be easily crushed and deformed by hands. G) Movement of the soft factor in eight directions within a 9 mm circle controlled by the four STMs. Scale bar—10 mm. Red color indicates the pressurized state, while the blue color indicates the depressurized state. H) The movement of the soft factor in the z-axis direction was controlled by the silicone balloon. Scale bar—5 mm. I) The maximum values of shear force in the four principal directions and normal force produced by the SS haptic device. J) The thermo-responsive VSS frame enhances the conformability of the SS haptic device to areas of complex geometries on the body such as the back of the hand. K) The LM soft tactile sensor and low-modulus stretchable wiring can be added underneath the soft factor for normal force monitoring.

the body with high conformability and comfort, as shown in Figure 9C,D. Figure 9F1–F3 displays images of the textile-based SS haptic device being highly flexible and soft, which can be easily crushed and deformed by hands without being damaged (Video, Supporting Information).

Characterization of the 3D SS haptic device was also conducted and is presented in Figure 9G–I (Video, Supporting Information). Experimental results in Figure 9G show the movements of the soft factor (6 mm in diameter) in eight directions within a 9 mm circle, which corresponds to a displacement of 1.5 mm in each direction. Results in Figure 9H also reveal that the silicone balloon could move the soft factor with a displacement of 3 mm in the z-axis direction. In addition to displacement, magnitudes of forces generated by the SS haptic device are also an important factor for inducing SS sensation. Therefore, they were also characterized by a six-axis ATI nano-17 force sensor (ATI Industrial Automation, USA), and the

maximum force values are displayed in Figure 9I. The results reveal that the SS haptic device can produce at least 1 N of shear force in each principal direction (i.e., the directions along the STMs), with the shear force in one direction being able to reach up to approximately 1.5 N. The difference in shear force values between directions can be attributed to the inconsistency with the fabrication process in the laboratory. It can also be expected that the shear forces along the diagonal directions can be higher than those of the four principal directions as two adjacent STMs are required to move the soft factor in the diagonal directions. The maximum normal force generated by the silicone balloon was also measured and could reach 1.72 N. These measured force values are comparable to those of other SS haptic devices in the literature.^[45b,47] It is worth noting that the shear force values reported earlier were measured with the normal force of approximately 0.6 N, which is slightly more than one-third of the maximum value that the silicone balloon can produce. As a result, to

improve the SS sensation, higher normal force values can still be used to improve the friction between the soft tactor and the skin, while the surface of the soft tactor can also be coated with a thin layer of adhesive for increased friction. In addition, the 3D SS haptic device presented in this study can also be equipped with a thermo-responsive VSS frame to improve its conformability to other areas of more complex geometries on the body (e.g., the back of the hand), as shown in Figure 9J. An LM soft tactile sensor with high sensitivity to pressure^[39a] connected with low-modulus stretchable wiring that can maintain stable conductance under tensile strain^[48] can also be added to the SS device for normal force monitoring (Figure 9K). These initial results have demonstrated the potential use of the STMs in creating a wearable 3D SS haptic device to effectively induce SS sensation to the wearers while maintaining their comfort, and potentially in other multifunctional smart textile structures for soft robotic and wearable applications.

3. Discussion and Conclusion

In this work, a new class of programmable STMs, which is referred to as STMs, has been presented. The proposed STMs are developed based on fluidic channels made from LM patterns embedded in silicone sheets, which are directly constrained by textiles and apparel engineering techniques, including computerized sewing processes, for desirable motions upon pressurization with fluid sources. This design and fabrication method for the STMs theoretically allows the creation of STMs with any desired channel designs and exhibits a high degree of suitability for automated manufacturing processes. Comprising entirely soft materials (e.g., silicone elastomers, textiles, stitches), these STMs are inherently compliant, highly conformable, and have a low-profile, planar form factor that enables seamless incorporation of additional components, including soft piezoresistive sensors, thermo-responsive VSSs, and stretchable conductors, to create advanced, multifunctional soft textile robotic systems. The applicability of the presented STMs is demonstrated by the design and fabrication of a completely soft, wearable 3D SS haptic device.

Thanks to being closely embedded to the fluidic channels, the soft piezoresistive sensors presented in this study possess an enhanced sensitivity to pressure-induced elongation of the STMs, which can be remarkably useful in closed-loop control. The thermo-responsive VSSs, fabricated by the injection method with either LMPAs or a new thermo-responsive epoxy with low viscosity and transition temperature, can be helpful in enhancing both the load-bearing capability of STMs and conformability of STM-based wearable devices. The wearable 3D SS haptic device developed based on STMs was highly conformable and could generate SS force comparable to other similar devices. It could also incorporate a thermo-responsive VSS frame for enhanced conformability, and soft sensors and stretchable conductors for feedback monitoring purposes. In addition to the prototypes demonstrated in this article, the STMs are also highly customizable to realize devices of various scales and made from a wide range of silicone elastomers (instead of depending on commercial elastic tubes or bladders) that can have different force and elongation capability to suit different applications. A comparison

between the STMs in this study and other types of planar fluidic textile actuators in the literature is also provided in Table S2, Supporting Information.

Despite showing promising results, these STMs still exhibit several limitations that need future investigation. The most notable one is their susceptibility to failure under high pressure, which is important to enhance their operating range. As the fluidic channels in this study are fabricated by encapsulating LM patterns with silicone, the interface between two silicone layers is relatively weak and susceptible to separation under high pressure, causing the STMs to fail. One potential solution to this issue is to employ other fabrication methods that do not involve encapsulation, such as the soft materials embedded 3D printing technique where fluidic channels can be created by directly printing inside a liquid silicone bath before it is cured and combined with textiles.

The STMs can also benefit from future improvement in the constraining textile layers where wrinkled textile structures (that can be made to accommodate higher stretchability) can be used for constraining, instead of commercial stretchable textiles. Additionally, selectively programming textile structures (e.g., selective wrinkling, or machine knitting) can also expand the potential of the STMs with greater programmability to achieve a larger variety of motions. Although the analytical model developed in this study can provide a good prediction of the STMs' pressure-induced elongation, the model is still quasi-static and relies on the assumption that the STMs operate within their linear elastic regime, which did not account for the hyperelastic behavior of constituent materials. The current model also depends on the assumption that the STMs undergo two phases during their elongation, which actually can occur simultaneously under hydraulic pressure. As a result, in future work, the development of a new and more complicated analytical model, based on the strain energy model for hyperelastic materials, and finite-element analysis can enable a better understanding of the deformation of the STMs under hydraulic pressure. Despite already possessing a low transition temperature, the VSSs in this work can be further enhanced by including a real-time temperature controller, which is based on miniature thermal sensors and a feedback control algorithm,^[49] to maintain the temperature just within the VSSs' soft states. This feature will be highly useful for VSSs to avoid overheating issues, enhance safety, and enable smooth operations. Future research is also needed on compact fluid power sources as they are an essential component for the development of STM-based wearable devices. In addition to the 3D SS haptic device demonstrated, the design and fabrication method of the STMs are also amenable to realizing other advanced, multifunctional smart textile structures for soft robotic and wearable applications, such as soft grippers, shape-changing structures, soft assistive devices, or haptic interfaces, which will be explored in the future work.

4. Experimental Section

Fabrication of STMs: The silicone sheets were fabricated by casting Dragon Skin Fx-Pro silicone elastomer (Smooth-On Inc., USA) mixed at a weight ratio of 1:1 (part A: part B) on a PTFE substrate using a thin-film applicator (ZUA 2000, Zehntner Inc., Switzerland). EGain liquid metal (75.5% Ga and 24.5% In by weight) was then patterned on silicone sheets

using either stamping or stencil-printing methods. In the stamping method, polydimethylsiloxane (PDMS) stamps with desired stamping features were created by molding PDMS in 3D-printed molds. A PDMS roller coated in LM was used to apply a thin layer of LM onto the protruding features of the stamps, and LM patterns were transferred by slightly pressing the stamps on the silicone sheets. In the stencil-printing method, stencils for LM patterns were first created by patterning thin PTFE films (approximately 0.076 mm thick, McMaster-Carr, USA) on a Silhouette cutting machine (Silhouette, USA). The stencils, after being fabricated, were cleaned with isopropanol swabs before they were applied to the cured silicone sheets. The same PDMS roller coated in LM was rolled over the stencils, forming LM patterns on the silicone sheets. Once successfully formed, LM patterns were encapsulated by another layer of silicone, and the silicone sheets were left to cure in the oven at 65 °C for 20 min. Textile layers were then bonded on both the top and bottom surfaces of the silicone sheets using a thin layer of liquid silicone, resulting in a silicone–textile composite sheet structure. Constraining zigzag stitches were then sewn around the LM patterns using a sewing machine (Janome, Japan), and fluid transmission tubes made from PTFE tubes were connected to the opening of the LM patterns for fluid supply. The connection between fluid transmission tubes and STMs was then reinforced by knots of polyester threads and superglue for a watertight seal. A syringe filled with water was connected to the other end of the fluid transmission tubes and used as the fluid source.

Mechanical Characterization of STMs: The experimental setup for characterization of the STMs consisted of a hydraulic source, a pressure sensor for hydraulic pressure monitoring, an optical encoder for measuring input volume, and either a laser displacement sensor for elongation testing or a miniaturized load cell for contraction force testing (Figure S2, Supporting Information). The hydraulic source employed a linear translational stage (Zaber Technologies, Canada) to push a syringe to pump water into the STM prototypes. The optical encoder (US Digital, USA) was placed in addition to the linear translational stage to track the displacement of the syringe plunger, which could then be converted into input volume. The pressure sensor (Honeywell, USA) was installed amid the fluid transmission tubes and the STM prototypes via a T connector to measure the hydraulic pressure. A 3D-printed fixture, laminated with PTFE films to minimize friction, was used to support the STM prototypes during their elongation. During characterization, one end of the STM prototypes was connected to the hydraulic source while the other end was attached with a 3D-printed marker. A Quanser QPiDe data acquisition device (Quanser, Canada) was used to record the readings of all components with the Simulink environment (MathWorks, USA).

In the elongation experiment, a laser displacement sensor (Keyence, USA) was placed opposite to the 3D-printed marker and measured the marker's displacement, which corresponds to the STM's elongation under hydraulic pressure. For contraction force characterization, the laser displacement sensor was replaced by a load cell (Futek, USA) that was connected with the STM prototype via an inextensible string with sufficient tension to prevent slacking during testing.

In the frequency response characterization, an experimental setup similar to that of the elongation experiment was employed, where the linear translational stage was programmed to apply sinusoidal driving signals of a range of frequencies, from 0.1 to 8 Hz, to the syringe plunger so that the STM prototype produced a fixed elongation of approximately 10%. The range of tested frequencies stops at 8 Hz because of the mechanical system limitation that could not generate driving signals with frequencies larger than 8 Hz. The same laser displacement sensor was used to measure the elongation values of the STM prototype at each frequency. The frequency response was evaluated by the reduction in the STM prototype's elongation at each frequency compared to the first one (i.e., 0.1 Hz) using the root-power quantity equation.

For the integrated piezoresistive sensor's characterization, the same experimental setup as the elongation experiment was employed. The laser displacement sensor was used to measure the STM's elongation under hydraulic pressure, and the resistance of the piezoresistive sensor was monitored by the readout circuit shown in Figure 7G, using a four-wire probe with a constant current of 0.1 A.

Analytical Model: Tensile modulus values for the silicone and textile used in the analytical model were obtained from the stress–strain curves of their samples (Figure S3, Supporting Information) tested on an Instron 5543 (Instron, USA) mechanical testing machine. Tensile modulus values were calculated with a linear fitting from 5% to 10% strain.

Stiffness Variation Characterization: The stiffness variation of the 832WC thermo-responsive epoxy was characterized using a bending cantilever experiment displayed in Figure S6, Supporting Information. Beam samples made from the thermo-responsive epoxy were fixed on a fixture, sticking out a length of $L = 13$ mm. A Mark-10 force gauge, controlled by the linear translational stage, was used to push against the beam samples by a distance of 1 mm. The flexural modulus values of the thermo-responsive epoxy could then be calculated by employing the cantilever beam model: $E = FL^3/3I\delta$, where E is the flexural modulus value to be determined, F is the force value read by the force gauge, δ is the deflection of the tip, and $I = bh^3/12$ is the second moment of inertia of the tested beam samples.

Supporting Information

Supporting Information is available from the Wiley Online Library or from the author.

Acknowledgements

The authors acknowledge the support from the UNSW Start-Up Grant (grant no. PS58173), the UNSW Scientia Fellowship Grant (grant no. PS46197-A), and the Vanguard Grant from the National Heart Foundation of Australia (grant no. RG204224). This was performed in part at the NSW Node of the Australian National Fabrication Facility. Trung Thien Hoang, Mai Thanh Thai, Chi Cong Nguyen, and Hien Anh Tran would like to acknowledge the support from the Science and Technology Scholarship Program for Overseas Study for Master's and Doctoral Degrees, Vin University, Vingroup, Vietnam.

Open access publishing facilitated by University of New South Wales, as part of the Wiley - University of New South Wales agreement via the Council of Australian University Librarians.

Conflict of Interest

The authors declare no conflict of interest.

Data Availability Statement

The data that support the findings of this study are available from the corresponding author upon reasonable request.

Keywords

haptics, liquid metals, shape programmables, smart textiles, soft sensors, soft textile muscles, variable stiffnesses

Received: December 18, 2023

Revised: February 19, 2024

Published online:

- [1] a) K. C. Galloway, K. P. Becker, B. Phillips, J. Kirby, S. Licht, D. Tchernov, R. J. Wood, D. F. Gruber, *Soft Rob.* **2016**, *3*, 23; b) J. Shintake, V. Cacucciolo, D. Floreano, H. Shea, *Adv. Mater.* **2018**, *30*, 1707035.

- [2] R. F. Shepherd, F. Ilievski, W. Choi, S. A. Morin, A. A. Stokes, A. D. Mazzeo, X. Chen, M. Wang, G. M. Whitesides, *Proc. Natl. Acad. Sci. U. S. A.* **2011**, *108*, 20400.
- [3] G. Mao, M. Drack, M. Karami-Mosammam, D. Wirthl, T. Stockinger, R. Schwödiauer, M. Kaltenbrunner, *Sci. Adv.* **2020**, *6*, eabc0251.
- [4] C. Chautems, A. Tonazzini, Q. Boehler, S. H. Jeong, D. Floreano, B. J. Nelson, *Adv. Intell. Syst.* **2020**, *2*, 1900086.
- [5] a) T. T. V. Doan, H. Sato, *J. Visualized Exp.* **2016**, e54260; b) T. V. Doan, Y. Li, F. Cao, H. Sato, presented at 2015 28th IEEE Int. Conf. Micro Electro Mechanical Systems (MEMS), IEEE, Piscataway, NJ, **2015**; c) Y. Li, F. Cao, T. T. V. Doan, H. Sato, *Bioinspiration Biomimetics* **2016**, *11*, 056018; d) H. D. Nguyen, V. T. Dung, H. Sato, T. T. Vo-Doan, *Sens. Actuators, B* **2023**, *376*, 132988; e) T. Shimomura, H. Iwamoto, T. T. V. Doan, S. I. Ishiwata, H. Sato, M. Suzuki, *Biophys. J.* **2016**, *111*, 1295.
- [6] a) K. Bark, J. Wheeler, G. Lee, J. Savall, M. Cutkosky, in Proc. - 3rd Joint EuroHaptics Conf. Symposium on Haptic Interfaces for Virtual Environment and Teleoperator Systems, World Haptics 2009, Salt Lake City, UT **2009**, <https://doi.org/10.1109/WHC.2009.4810850464>; b) J. B. Chossat, D. K. Y. Chen, Y. L. Park, P. B. Shull, *IEEE Trans. Haptics* **2019**, *12*, 521.
- [7] P. Polygerinos, Z. Wang, K. C. Galloway, R. J. Wood, C. J. Walsh, *Rob. Auton. Syst.* **2015**, *73*, 135.
- [8] a) L. Sy, T. T. Hoang, M. Bussu, M. T. Thai, P. T. Phan, H. Low, D. Tsai, M. A. Brodie, N. H. Lovell, T. N. Do, presented at 2021 IEEE 4th Int. Conf. Soft Robotics (RoboSoft), IEEE, Piscataway, NJ, April **2021**; b) T. T. Hoang, L. Sy, M. Bussu, M. T. Thai, H. Low, P. T. Phan, J. Davies, C. C. Nguyen, N. H. Lovell, T. N. Do, *Sensors* **2021**, *21*, 7638.
- [9] a) J. Yang, K. Y. Kwon, S. Kanetkar, R. Xing, P. Nithyanandam, Y. Li, W. Jung, W. Gong, M. Tuman, Q. Shen, *Adv. Mater. Technol.* **2022**, *7*, 2101074; b) J. Yang, P. Nithyanandam, S. Kanetkar, K. Y. Kwon, J. Ma, S. Im, J. H. Oh, M. Shamsi, M. Wilkins, M. Daniele, *Adv. Mater. Technol.* **2023**, *8*, 2202183; c) V. K. Truong, A. Hayles, R. Bright, T. Q. Luu, M. D. Dickey, K. Kalantar-Zadeh, K. Vasilev, *ACS Nano* **2023**, *17*, 14406; d) T.-K. Nguyen, M. Barton, A. Ashok, T.-A. Truong, S. Yadav, M. Leitch, T.-V. Nguyen, N. Kashaninejad, T. Dinh, L. Hold, *Proc. Natl. Acad. Sci.* **2022**, *119*, e2203287119; e) T.-K. Nguyen, S. Yadav, T.-A. Truong, M. Han, M. Barton, M. Leitch, P. Guzman, T. Dinh, A. Ashok, H. Vu, *ACS Nano* **2022**, *16*, 10890; f) T. Nguyen, T. Dinh, C.-D. Tran, H.-P. Phan, T.-K. Nguyen, H. K. Nguyen, F. A. Riduan, P. Guzman, N.-T. Nguyen, D. V. Dao, *IEEE Sens. J.* **2020**, *21*, 7308; g) T.-K. Nguyen, H.-P. Phan, H. Kamble, R. Vadivelu, T. Dinh, A. Iacopi, G. Walker, L. Hold, N.-T. Nguyen, D. V. Dao, *ACS Appl. Mater. Interfaces* **2017**, *9*, 41641; h) T. Nguyen, T. Dinh, H.-P. Phan, T.-K. Nguyen, A. R. M. Foisal, N.-T. Nguyen, D. V. Dao, *J. Mater. Chem. C* **2020**, *8*, 4713; i) T. Dinh, T. Nguyen, A. Foisal, H.-P. Phan, T.-K. Nguyen, N.-T. Nguyen, D. Dao, *Sci. Adv.* **2020**, *6*, eaay2671; j) S. Peng, S. Wu, Y. Yu, Z. Sha, G. Li, T. T. Hoang, M. T. Thai, T. N. Do, D. Chu, C. H. Wang, *J. Mater. Chem. A* **2021**, *9*, 26788; k) N.-K. Nguyen, T. Nguyen, T.-K. Nguyen, S. Yadav, T. Dinh, M. K. Masud, P. Singha, T. N. Do, M. J. Barton, H. T. Ta, *ACS Appl. Electron. Mater.* **2021**, *3*, 1959.
- [10] a) T. L. Buckner, R. A. Bilodeau, S. Y. Kim, R. Kramer-Bottiglio, *Proc. Natl. Acad. Sci. U. S. A.* **2020**, *117*, 25360; b) V. Sanchez, C. J. Walsh, R. J. Wood, *Adv. Funct. Mater.* **2021**, *31*, 2008278; c) C. C. Nguyen, S. Wong, M. T. Thai, T. T. Hoang, P. T. Phan, J. Davies, L. Wu, D. Tsai, H. P. Phan, N. H. Lovell, *Adv. Sens. Res.* **2023**, *2*, 2200036.
- [11] a) F. A. Panizzolo, I. Galiana, A. T. Asbeck, C. Sivi, K. Schmidt, K. G. Holt, C. J. Walsh, *J. NeuroEng. Rehabil.* **2016**, *13*, 43; b) Y. Ding, I. Galiana, A. Asbeck, B. Quinlivan, S. M. M. De Rossi, C. Walsh, in 2014 IEEE Int. Conf. Robotics and Automation (ICRA), IEEE, Piscataway, NJ, May **2014**.
- [12] B. B. Kang, H. Choi, H. Lee, K. J. Cho, *Soft Rob.* **2019**, *6*, 214.
- [13] C. Rognon, V. Ramachandran, A. R. Wu, A. J. Ijspeert, D. Floreano, *IEEE Trans. Haptics* **2019**, *12*, 375.
- [14] a) T. N. Do, T. Tjahjowidodo, M. W. S. Lau, S. J. Phee, presented at ICINCO 2013 - Proc. 10th Int. Conf. Informatics in Control, Automation and Robotics, 2013, Reykjavik, Iceland **2013**; b) T. N. Do, T. E. T. Seah, S. J. Phee, *IEEE Trans. Biomed. Eng.* **2016**, *63*, 1229; c) H. M. Le, T. N. Do, S. J. Phee, *Sens. Actuators, A* **2016**, *247*, 323.
- [15] R. Granberry, K. Eschen, B. Holschuh, J. Abel, *Adv. Mater. Technol.* **2019**, *4*, 1900548.
- [16] J. H. H. Kim, K. Huang, S. White, M. Conroy, C. H. L. Kao, in *DIS 2021 - Proc. 2021 ACM Designing Interactive Systems Conf.: Nowhere and Everywhere 2021*, New York, NY **2021**, p. 1183.
- [17] C. S. Haines, M. D. Lima, N. Li, G. M. Spinks, J. Foroughi, J. D. W. Madden, S. H. Kim, S. Fang, M. J. De Andrade, F. Göktepe, Ö. Göktepe, S. M. Mirvakili, S. Naficy, X. Lepró, J. Oh, M. E. Kozlov, S. J. Kim, X. Xu, B. J. Swedlove, G. G. Wallace, R. H. Baughman, *Science* **2014**, *343*, 868.
- [18] L. Cappello, K. C. Galloway, S. Sanan, D. A. Wagner, R. Granberry, S. Engelhardt, F. L. Haufe, J. D. Peisner, C. J. Walsh, *Soft Rob.* **2018**, *5*, 662.
- [19] a) C. Correia, K. Nuckols, D. Wagner, Y. M. Zhou, M. Clarke, D. Orzel, R. Solinsky, S. Paganoni, C. J. Walsh, *IEEE Trans. Neural Syst. Rehabil. Eng.* **2020**, *28*, 1407; b) Y. M. Zhou, D. Wagner, K. Nuckols, R. Heimgartner, C. Correia, M. Clarke, D. Orzel, C. O'Neill, R. Solinsky, S. Paganoni, C. J. Walsh, presented at 2019 Int. Conf. Robotics and Automation (ICRA), Montreal, QC, Canada, May **2019**; c) P. T. Phan, T. T. Hoang, M. T. Thai, H. Low, N. H. Lovell, T. N. Do, *Soft Rob.* **2022**, *9*, 820.
- [20] a) P. T. Phan, T. T. Hoang, M. T. Thai, H. Low, J. Davies, N. H. Lovell, T. N. Do, *Sci. Rep.* **2021**, *11*, 22420; b) M. T. Thai, P. T. Phan, T. T. Hoang, H. Low, N. H. Lovell, T. N. Do, *IEEE Rob. Autom. Lett.* **2021**, *6*, 5089.
- [21] a) B. Tondu, P. Lopez, *IEEE Control Syst.* **2000**, *20*, 15; b) F. Daerden, D. Lefeber, *Eur. J. Mech. Environ. Eng.* **2002**, *47*, 10; c) S. Davis, D. G. Caldwell, *Int. J. Rob. Res.* **2006**, *25*, 359.
- [22] a) M. Wehner, B. Quinlivan, P. M. Aubin, E. Martinez-Villalpando, M. Baumann, L. Stirling, K. Holt, R. Wood, C. Walsh, in 2013 IEEE Int. Conf. Robotics and Automation, IEEE, Piscataway, NJ, May **2013**; b) Y. L. Park, B. R. Chen, N. O. Pérez-Arancibia, D. Young, L. Stirling, R. J. Wood, E. C. Goldfield, R. Nagpal, *Bioinspiration Biomimetics* **2014**, *9*, 016007; c) G. Belforte, G. Eula, A. Ivanov, T. Raparelli, S. Sirolli, *J. Text. Inst.* **2018**, *109*, 757; d) H. Li, J. Yao, P. Zhou, W. Zhao, Y. Xu, Y. Zhao, *Bioinspiration Biomimetics* **2020**, *15*, 026006; e) E. T. Roche, M. A. Horvath, I. Wamala, A. Alazmani, S. E. Song, W. Whyte, Z. Machaidze, C. J. Payne, J. C. Weaver, G. Fishbein, J. Kuebler, N. V. Vasilyev, D. J. Mooney, F. A. Pigula, C. J. Walsh, *Sci. Transl. Med.* **2017**, *9*, eaaf3925.
- [23] a) E. J. Ball, M. A. Meller, J. B. Chipka, E. Garcia, *Smart Mater. Struct.* **2016**, *25*, 115024; b) G. Belforte, G. Eula, A. Ivanov, T. Raparelli, S. Sirolli, presented at Advances in Service and Industrial Robotics, Cham **2018**.
- [24] N. D. Naclerio, E. W. Hawkes, *IEEE Rob. Autom. Lett.* **2020**, *5*, 3406.
- [25] a) E. W. Hawkes, D. L. Christensen, A. M. Okamura, in Proc. - IEEE Int. Conf. Robotics and Automation, IEEE, Piscataway, NJ, June **2016**, p. 4022; b) P. T. Phan, M. T. Thai, T. T. Hoang, N. H. Lovell, T. N. Do, *IEEE Access* **2020**, *8*, 226637; c) M. T. Thai, P. T. Phan, H. A. Tran, C. C. Nguyen, T. T. Hoang, J. Davies, J. Rnjak-Kovacina, H. P. Phan, N. H. Lovell, T. N. Do, *Adv. Sci.* **2023**, *10*, 2205656.

- [26] a) R. Niiyama, D. Rus, S. Kim, in Proc. - IEEE Int. Conf. Robotics and Automation, IEEE, Piscataway, NJ, **2014**, <https://doi.org/10.1109/ICRA.2014.69077936332>; b) R. Niiyama, X. Sun, C. Sung, B. An, D. Rus, S. Kim, *Soft Rob.* **2015**, 2, 59; c) S.-H. Park, J. Yi, D. Kim, Y. Lee, H. S. Koo, Y.-L. Park, in 2019 2nd IEEE Int. Conf. Soft Robotics (RoboSoft), IEEE, Piscataway, NJ, April **2019**; d) C. M. Thalman, L. Baye-Wallace, H. Lee, in 2021 IEEE/RSJ Int. Conf. Intelligent Robots and Systems (IROS), IEEE, Piscataway, NJ, September **2021**.
- [27] a) H. Lee, N. Oh, H. Rodrigue, *IEEE Rob. Autom. Mag.* **2020**, 27, 65; b) P. H. Nguyen, I. B. Imran Mohd, C. Sparks, F. L. Arellano, W. Zhang, P. Polygerinos, presented at 2019 Int. Conf. Robotics and Automation (ICRA), Montreal, QC, Canada, May **2019**.
- [28] M. Zhu, T. N. Do, E. Hawkes, Y. Visell, *Soft Rob.* **2020**, 7, 179.
- [29] a) Y. Funabora, in IEEE Int. Conf. Intelligent Robots and Systems, IEEE, Piscataway, NJ **2018**, <https://doi.org/10.1109/IROS.2018.85943596992>; b) T. Abe, S. Koizumi, H. Nabae, G. Endo, K. Suzumori, N. Sato, M. Adachi, F. Takamizawa, *IEEE Rob. Autom. Lett.* **2019**, 4, 2532; c) S. Kurumaya, H. Nabae, G. Endo, K. Suzumori, *Soft Rob.* **2019**, 6, 250.
- [30] a) O. Kilic Afsar, A. Shtarbanov, H. Mor, K. Nakagaki, J. Forman, K. Modrei, S. H. Jeong, K. Hjort, K. Höök, H. Ishii, in 34th Annual ACM Symposium On User Interface Software and Technology, New York, NY, October **2021**; b) P. T. Phan, D. Welch, J. Spiggle, M. T. Thai, T. T. Hoang, J. Davies, C. C. Nguyen, K. Zhu, H.-P. Phan, N. H. Lovell, *Sens. Actuators, A* **2023**, 360, 114555; c) P. T. Phan, M. T. Thai, T. T. Hoang, J. Davies, C. C. Nguyen, H.-P. Phan, N. H. Lovell, T. N. Do, *Sci. Rep.* **2022**, 12, 11067; d) J. Davies, M. T. Thai, H. Low, P. T. Phan, T. T. Hoang, N. H. Lovell, T. N. Do, *Soft Rob.* **2023**, 10, 1055.
- [31] J. Davies, M. T. Thai, T. T. Hoang, C. C. Nguyen, P. T. Phan, H. P. Phan, N. H. Lovell, T. N. Do, *Adv. Mater. Technol.* **2023**, 8, 2201453.
- [32] a) V. Sanchez, C. J. Payne, D. J. Preston, J. T. Alvarez, J. C. Weaver, A. T. Atalay, M. Boyvat, D. M. Vogt, R. J. Wood, G. M. Whitesides, C. J. Walsh, *Adv. Mater. Technol.* **2020**, 5, 2000383; b) M. Zhu, A. H. Memar, A. Gupta, M. Samad, P. Agarwal, Y. Visell, S. J. Keller, N. Colonnese, in Conf. Human Factors in Computing Systems – Proc., New York, NY **2020**, <https://doi.org/10.1145/3313831.33763331>.
- [33] a) A. D. Marchese, R. K. Katschmann, D. Rus, *Soft Rob.* **2015**, 2, 7; b) M. De Volder, D. Reynaerts, *J. Micromech. Microeng.* **2010**, 20, 043001.
- [34] S. Y. Tang, C. Tabor, K. Kalantar-Zadeh, M. D. Dickey, *Annu. Rev. Mater. Res.* **2021**, 51, 381.
- [35] K. Doudrick, S. Liu, E. M. Mutunga, K. L. Klein, V. Damle, K. K. Varanasi, K. Rykaczewski, *Langmuir* **2014**, 30, 6867.
- [36] J. Wirekoh, Y.-L. Park, *Smart Mater. Struct.* **2017**, 26, 035009.
- [37] Y.-L. Park, J. Santos, K. G. Galloway, E. C. Goldfield, R. J. Wood, in 2014 IEEE Int. Conf. Robotics and Automation (ICRA), IEEE, Piscataway, NJ, May 2014.
- [38] S. Park, K. Mondal, R. M. Treadway, V. Kumar, S. Ma, J. D. Holbery, M. D. Dickey, *ACS Appl. Mater. Interfaces* **2018**, 10, 11261.
- [39] a) T. T. Hoang, P. T. Phan, M. T. Thai, N. H. Lovell, T. N. Do, *Adv. Mater. Technol.* **2020**, 5, 2000724; b) T. T. Hoang, J. J. S. Quek, M. T. Thai, P. T. Phan, N. H. Lovell, T. N. Do, *Sens. Actuators, A* **2021**, 323, 112673.
- [40] a) Y. Hao, T. Wang, X. Fang, K. Yang, L. Mao, J. Guan, L. Wen, in Chinese Control Conference, CCC, Dalian, China **2017**, <https://doi.org/10.23919/ChiCC.2017.80284276781>; b) J. Shintake, B. Schubert, S. Rosset, H. Shea, D. Floreano, in 2015 IEEE/RSJ Int. Conf. Intelligent Robots and Systems (IROS), IEEE, Piscataway, NJ, September **2015**.
- [41] T. L. Buckner, M. C. Yuen, S. Y. Kim, R. Kramer-Bottiglio, *Adv. Funct. Mater.* **2019**, 29, 1903368.
- [42] <https://miller-stephenson.com/product/epon-828/> (accessed: March 2024).
- [43] <https://mgchemicals.com/products/potting-compounds/epoxy-potting/clear-epoxy-resin/> (accessed: March 2024).
- [44] J. Wheeler, K. Bark, J. Savall, M. Cutkosky, *IEEE Trans. Neural Syst. Rehabil. Eng.* **2010**, 18, 58.
- [45] a) A. L. Guinan, N. C. Hornbaker, M. N. Montandon, A. J. Doxon, W. R. Provancher, in 2013 World Haptics Conf., WHC 2013, Daejeon, Korea (South) **2013**, <https://doi.org/10.1109/WHC.2013.654837713>; b) M. T. Thai, T. T. Hoang, P. T. Phan, N. H. Lovell, T. N. Do, *IEEE Access* **2020**, 8, 157878.
- [46] Y. H. Jung, J.-Y. Yoo, A. Vázquez-Guardado, J.-H. Kim, J.-T. Kim, H. Luan, M. Park, J. Lim, H.-S. Shin, C.-J. Su, R. Schloen, J. Trueb, R. Avila, J.-K. Chang, D. S. Yang, Y. Park, H. Ryu, H.-J. Yoon, G. Lee, H. Jeong, J. U. Kim, A. Akhtar, J. Cornman, T.-I. Kim, Y. Huang, J. A. Rogers, *Nat. Electron.* **2022**, 5, 374.
- [47] K. T. Yoshida, C. M. Nunez, S. R. Williams, A. M. Okamura, M. Luo, in 2019 IEEE World Haptics Conf., WHC 2019, IEEE, Piscataway, NJ **2019**, <https://doi.org/10.1109/WHC.2019.881608497>.
- [48] T. T. Hoang, P. T. Phan, M. T. Thai, J. Davies, C. C. Nguyen, H.-P. Phan, N. H. Lovell, T. N. Do, *Adv. Intell. Syst.* **2022**, 4, 2200282.
- [49] T. Hoang, B. H. Ly, T. X. Le, T. T. Huynh, H. T. Nguyen, T. Van Vo, T. T. H. Pham, K. Huynh, *Microsyst. Technol.* **2020**, 26, 1863.